Visible Light-Induced Room-Temperature Formaldehyde Gas Sensor Based on Porous Three-Dimensional ZnO Nanorod Clusters with Rich Oxygen Vacancies

Bo Zhang, Jing Wang,* Qufu Wei, Pingping Yu, Shuai Zhang, Yin Xu, Yue Dong, Yi Ni, Jinping Ao, and Yi Xia*

Read Online

ACCESS | 📊 Metrics & More | 📖 Article Recommendations | 📄 Supporting Information

ABSTRACT: Oxygen vacancy (V_O) is a kind of primary point defect that extensively exists in semiconductor metal oxides (SMOs). Owing to some of its inherent qualities, an artificial manipulation of V_O content in one material has evolved into a hot research field, which is deemed to be capable of modulating band structures and surface characteristics of SMOs. Specific to the gas-sensing area, V_O engineering of sensing materials has become an effective means in enhancing sensor response and inducing light-enhanced sensing. In this work, a high-efficiency microwave hydrothermal treatment was utilized to prepare a V_O-rich ZnO sample without additional reagents. The X-ray photoelectron spectroscopy test revealed a significant increase in V_O proportion, which was from 9.21% in commercial ZnO to 36.27% in synthesized V_O-rich ZnO possessing three-dimensional and air-permeable microstructures. The subsequent UV−vis−NIR absorption and photoluminescence spectroscopy indicated an extension absorption in the visible region and band gap reduction of V_O-rich ZnO. It turned out that the V_O-rich ZnO-based sensor exhibited a considerable response of 63% toward 1 ppm HCHO at room temperature (RT, 25 °C) under visible light irradiation. Particularly, the response/recovery time was only 32/20 s for 1 ppm HCHO and further shortened to 10/5 s for 10 ppm HCHO, which was an excellent performance and comparable to most sensors working at high temperatures. The results in this work strongly suggested the availability of V_O engineering and also provided a meaningful candidate for researchers to develop high-performance RT sensors detecting volatile organic compounds.
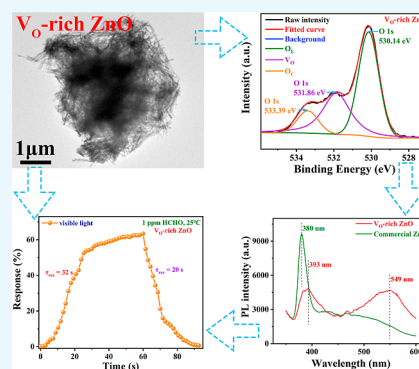
1. INTRODUCTION

At the present time, room-temperature (RT) gas sensing is occupying an important position. Researchers have exploited varieties of fresh theories, techniques, and materials to accelerate the progress in this field. However, to the best of our knowledge, RT sensing concentrates more upon several target gases with intrinsically high activity, especially NO_2,[1−4] NH_3,[5−7] H_2S,[8−10] and so forth.

Comparatively speaking, even now, high-temperature sensing on almost all volatile organic compounds (VOCs) is still mainstream and ingrained. For example, Zhang et al.[11] prepared hollow ZnO nanocages derived from ZIF-8, which exhibited a high response of 139.41 toward 100 ppm ethanol at 325 °C. Besides, it possessed an ultrashort response time (2.8 s) and low detection limit (25 ppb). Chang et al.[12] synthesized 2D WO_3 nanosheets by annealing inorganic fullerene-like WS_2 nanoparticles at different temperatures. The optimal WO_3 nanosheets, annealed at 500 °C, showed a response of 2.23 toward 0.17 ppm acetone at 300 °C, the response and recovery time being 6 and 10 s, respectively. Li et al.[13] transformed bead-like WO_3 fibers to hierarchical $WO_3/ZnWO_4$ 1D composites with the introduction of ZIF-8 into the precursor solution. The resulting $WO_3/ZnWO_4$-5% composites displayed a response of

44.5 toward 5 ppm HCHO at 220 °C. Meanwhile, the composites exhibited a short response/recovery time (12/14 s) and excellent stability. As we can see, high temperature endows VOC sensing with excellent performance and undeniably plays an important role in this process.

In contrast, although having made some progress, performance indicators regarding RT sensing on VOCs are far from satisfactory. For example, Kuchi et al.[14] developed a novel RT ethanol sensor based on PbS/SnS_2 nanocomposites via a simple method. Although the optimal PbS/SnS_2 (1:1)-based sensor showed good selectivity toward ethanol, the corresponding response was rather low, being 45.64−100.3% toward 60−1600 ppm ethanol. In particular, the sensor response and response/recovery time of PbS/SnS_2 (1:1) toward 800 ppm ethanol were ∼90% and 128/69 s, respectively. Vishwakarma et al.[15] applied

CdS-doped TiO_2 nanocomposites to RT acetone detection. However, an optimized 2 wt % CdS doping only made the composite show a response of 71% toward 5000 ppm acetone, the response/recovery time being 55/115 s. David et al.[16] demonstrated a RT Ag/Bi_2O_3 nanocomposite-based toluene gas sensor which had a detection range of 10−100 ppm. To be specific, its response toward 50 ppm toluene was 89.21%, and the corresponding response/recovery time was ∼60/∼320 s. It serves to show that relevant research on RT sensing toward VOCs is in a fledging period and woefully inadequate, which is exactly the driving force for us to carry out targeted research.

Without the booster action of high temperature on activating reactions, light irradiation, particularly, ultraviolet (UV) and visible light, is the most effective alternative means known to exert a comparable character in inducing carrier separation and deepening the reaction level. For one semiconductor, it can be light-activated only if photon energy exceeds the band gap barrier, resulting in the generation of electron−hole pairs.[17−19] For UV irradiation with short wavelengths (10−400 nm), high photon energy makes it capable of activating any semiconductors. In contrast, from the view of theoretical calculation, visible light (400−780 nm) can only activate finite semiconductors whose band gaps do not exceed 3.1 eV (400 nm).[20] Despite the seeming superiority for UV irradiation, irreversible damage brought by high-energy UV photons on device durability and human health has long been questioned. In addition, UV irradiation accounts for less than 5% of all solar spectra,[21] which is far less than visible light (>50%).

In the photoexcitation field, semiconductors can roughly be classified into two categories. SnO_2 (∼3.6 eV),[22] ZnO (∼3.37 eV),[23,24] and TiO_2 (∼3.2 eV)[21,22] are usually identified as wide band gap semiconductors. Given that the ultimate activation band gap for visible light is, as abovementioned, 3.1 eV, wide band gap oxides listed above can only be activated through UV irradiation but show no photoresponse to visible light. Correspondingly, In_2O_3 (∼2.8 eV),[25] WO_3 (∼2.8 eV),[26] CdS (∼2.4 eV),[21,27] SnS_2 (∼2.3 eV),[28] α-Fe_2O_3 (∼2.1 eV),[29,30] Co_3O_4 (∼2.1 eV),[31,32] In_2S_3 (2∼3 eV),[21,33] CdSe (∼1.7 eV),[34−36] InP (∼1.35 eV),[37,38] CuO (∼1.2 eV),[39] MoS_2 (∼1.2 eV),[40] and PbS (∼0.41 eV)[21,27,41] are generally regarded as narrow band gap semiconductors. Distinctly, narrow band gap oxides/sulfides can easily be activated by partial- or full-wave band of visible light. However, although narrow band gaps give rise to a better absorbance to visible light, the inevitably easier recombination of photogenerated electron/hole pairs results in low sensitivity and poor selectivity when such semiconductors are applied as gas-sensitive materials.[42] In contrast, wide band gap semiconductors, including their composites, are more suitable to serve as candidates for photoexcitation-aided gas sensors. To make the most of solar energy, especially harmless visible spectra, researchers are inclined to moderately modify wide band gap semiconductors to extend their photoresponse range into the visible light region. In this process, metals,[43−45] narrow band gap semiconductors,[21,27,28,38,46−52] carbon-based materials,[53−55] or others[56,57] are extensively utilized, which act as the so-called "sensitizers".[21,27,35,37,38,45,50−53,56,57]

V_O has been widely recognized and practically utilized to modulate the electronic and surface properties of metal oxides,[58−70] which effectively improves gas-sensing performances of chemiresistor-type sensors. There exist three basic consensuses for the roles played by V_O in material behaviors. First, V_O, possessing abundant localized electrons, generally acts as an electron donor[59,60,62,65−67,69,70] and manipulates the

carrier density (bulk resistance) of semiconductor materials,[59,60,62] especially for n-type metal oxides. As interfacial defects, the electron-rich nature of oxygen vacancies will facilitate the adsorption of O_2 molecules and increase the content of chemisorbed oxygen species.[58−60,63−67] In addition, V_O is also considered to serve as active sites for target gas adsorption.[58−60,62,64−68,70] Second, V_O can regulate band structures of semiconductor oxides and usually narrow their band gaps.[58−63,67,69,70] Furthermore, band gaps can be continually diminished with increasing V_O contents in oxides.[62] A narrower band gap means lower energy is required for electron transition. Therefore, V_O has also been applied to extend the photoexcitation range of wide band gap semiconductors to the visible spectrum.[58−60,62,69,70] Compared to the abovementioned "sensitizers", engineering (self-doping) of V_O is deemed as the most straightforward and ideal way of expanding the excitation range of semiconductors without introducing impurities or changing their intrinsic structures.[59,60,62,70] Third, V_O can trap photoinduced electrons and prompt the separation of photo-generated electron/hole pairs.[58,60,69,70] Through greatly extending the lifetime of activated carriers, V_O favors the charge-transfer efficiency in bulk materials.[58,60,67,69,70] Besides, the concomitance of isolated energy levels with V_O promotes light absorption.[60,62] In conclusion, V_O engineering is highly conducive to generating outstanding visible light-catalyzed gas-sensing performance.

Inspired by the abovementioned discussion, in this work, taking ZnO with an intrinsic wide band gap as the basis material, microwave heating treatment was adopted to enrich its V_O content. First, the band gap decrease and light absorption range expansion of the as-prepared ZnO sample were verified when taking commercial ZnO as a reference. Furthermore, with the aid of visible light irradiation, high-performance HCHO sensing at RT was achieved by V_O-rich ZnO. The critical role of V_O in this process was consolidated when making comparison with the sensing performance of commercial ZnO toward HCHO with or without visible light irradiation. Other light-activated RT HCHO sensing performance of V_O-rich ZnO was then presented and discussed in detail.

2. EXPERIMENTAL SECTION

2.1. Materials. All experimental materials such as zinc hydroxide ($Zn(OH)_2$), zinc acetate dihydrate ($Zn(CH_3COO)_2\cdot 2H_2O$), sodium hydroxide (NaOH), and ethanol were of analytical grade or above and used as received without further purification. Commercial ZnO in this work referred to ZnO nanopowders purchased from Shanghai Aladdin Biochemical Technology Co., Ltd.

2.2. Synthesis of V_O-Rich ZnO Nanorod Clusters. First, ZnO nanoseeds were obtained by adding NaOH ethanol solution into $Zn(CH_3COO)_2\cdot 2H_2O$ ethanol solution, which was vigorously stirred for 1 h at RT. Then, 2.0 g of ε-$Zn(OH)_2$ and 0.3 g of the synthesized ZnO nanoseeds were added separately into 40 mL of deionized water. The obtained suspension was aged and kept under microwave heating at 80 °C for 5 min for the growth of V_o-rich ZnO nanorod clusters. The obtained samples were washed and dried at 60 °C overnight for subsequent tests.

2.3. Characterizations. The powder X-ray diffraction (XRD) characterization for phase identification was performed on a Rigaku D/max-2550 X-ray diffractometer with high-intensity Cu Kα (λ = 0.154 nm) radiation in the range of 5−90°. The field emission scanning electron microscopy (FESEM)

characterization for morphological and microstructural evaluation was obtained on a ZEISS Gemini300 microscope operating at 15 kV. The transmission electron microscopy (TEM) and high-resolution TEM (HRTEM) characterizations for interfacial and crystallographic analysis were examined on a JEOL (JEM-2100F) microscope with an accelerating voltage of 200 kV. The X-ray photoelectron spectroscopy (XPS) characterization for chemical state recognition was conducted on an EscaLab Xi + photoelectron spectrometer. UV−vis−NIR diffuse reflectance spectra for band gap estimation were acquired on a PerkinElmer Lambda 950 UV−vis−NIR spectrophotometer. Photoluminescence (PL) spectra for defect level speculation were tested on a Hitachi F-7000 luminescence spectrometer using a Xe lamp with an excitation wavelength of 325 nm. The specific surface area of the sample was calculated through the Brunauer−Emmett−Teller (BET) equation based on the nitrogen adsorption isotherm, which was measured on a Micromeritics Gemini VII apparatus (surface area and porosity system) with prior degassing of the product under vacuum at 120 °C overnight.

2.4. Fabrication and Measurement of Gas Sensors. *2.4.1. Sensor Fabrication and Its Structure Parameters.* The batch of sensor devices adopted in this work was planar gas sensors integrated with interdigital electrodes, routinely applied in RT detection and manufactured via micro−nano machining technology. The device substrate (6*4*0.5 mm) was monocrystalline silicon wafer covered with a growing SiO_2 dielectric layer (300 nm thick). On the substrate surface, interdigital electrodes (finger width 20 μm, finger gap 20 μm, finger length 1.5 mm, and finger pairs 25) were patterned by the photolithography technique, and chromium/gold (Cr/Au, 10 nm/100 nm-thick) electrodes were then deposited by RF sputtering and a lift-off process.

After the completion of planar sensor fabrication, the device surface was set about to be coated with the as-prepared sensing materials. A suspension of the sample was first prepared through a dispersion and ultrasound treatment of ZnO powders in absolute ethanol. The suspension was then spin-coated onto interdigital electrodes and dried at 80 °C overnight to obtain integrated sensors.

2.4.2. Measurement of Gas Sensors. Gas-sensing properties of ZnO samples were evaluated through a self-built gas-sensing test system under laboratory conditions (20% RH, RT).

a. For the gas supply section, the construction of the dynamic test system was simulated, where a flowing target gas filled the whole gas piping. Gas sources, for example, HCHO, and the carrier gas, drying air, were stored in individual cylinders. Under the premise of ensuring a total flow constant (200 mL/min), diluted target gases with particular concentrations were obtained through accurately adjusting the flow rate ratio of two components via gas flowmeters.

b. For the signal acquisition section, the planar device coated with sensitive materials was integrated with the sensor base installed in the test platform. The sensor reacted with target gases in an enclosed space sealed by a quartz cover. Synchronously, the sensor signal was recorded and transmitted back to the data collector terminal through a desktop multimeter (Keithley 2700). The panoramic and enlarged photographs of the signal acquisition section are provided in Figure S1.

c. For the optical irradiation section, a xenon lamp with an ultraviolet cutoff filter was applied as the visible light source (λ > 420 nm, distance to sensor: 20 cm, and light intensity: 1.2 mW cm^{-2}). The illumination power could be manually adjusted using an optical attenuator and measured by means of a digital optical power meter (THORLABS, PM16-120).

For the case of n-type sensing materials (e.g., ZnO) and reducing target gases (e.g., HCHO), the sensor response was defined as S (%) = $(I_g - I_a)/I_a$*100% (I_a and I_g were the dynamically stabilized currents of ZnO sensors in air and in HCHO (reaching equilibrium), respectively) in this work. In addition, the time when current change reached 90% during response and recovery processes was defined as the response time (τ_{res}) and recovery time (τ_{rec}), respectively.

3. RESULTS AND DISCUSSION

3.1. Structural and Morphological Characteristics. The XRD test was conducted in the first place to confirm the substance composition and crystallinity of the as-prepared sample. As displayed in Figure 1, the recorded diffraction peaks
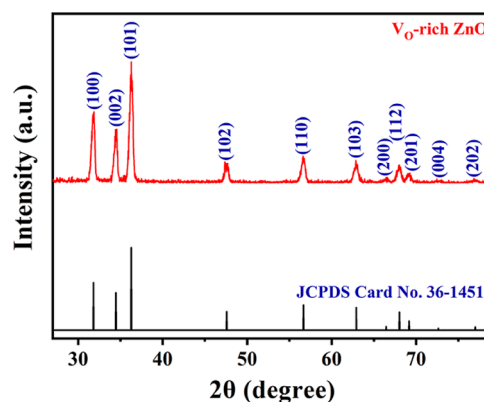

**Figure 1.** XRD patterns of the synthesized V_O-rich ZnO.

of V_O-rich ZnO could be well-assigned to the hexagonal phase of zinc oxide with lattice constants of a = 3.25 Å and c = 5.21 Å (standard JCPDS card no. 36-1451). Furthermore, all XRD diffraction peaks of V_O-rich ZnO were sharp and strong, revealing its high crystallization degree. In addition, none of the diffraction peaks derived from other impurities could be detected, which indicated the high purity of the product.

The microscopic structure and morphology of one material can influence and even determine its performance in most cases. Therefore, having a good grasp of microstructures of the as-prepared ZnO product is of great significance to foresee and analyze the gas-sensing properties. As shown in Figure 2a,b, scanning electron microscopy (SEM) characterization made clear that the obtained V_O-rich ZnO was composed of 3D clusters with inhomogenous shapes and sizes. Diameters of the observed agglomerations ranged from less than 5 μm to greater than 10 μm. In high-resolution Figures 2c,d and S2, individual clusters were cumulated by a mass of short ZnO nanorods with lengths of about 1 μm and diameters of about 35 nm. As we could see, ZnO nanorods arranged loosely side by side or intertwined each other in confusion, leaving much interspace inside the agglomerations. In Figure 2e, the V_O-rich ZnO cluster in TEM view showed a similar appearance to that in SEM. What mattered more was that the typical ZnO cluster in Figure 2e took
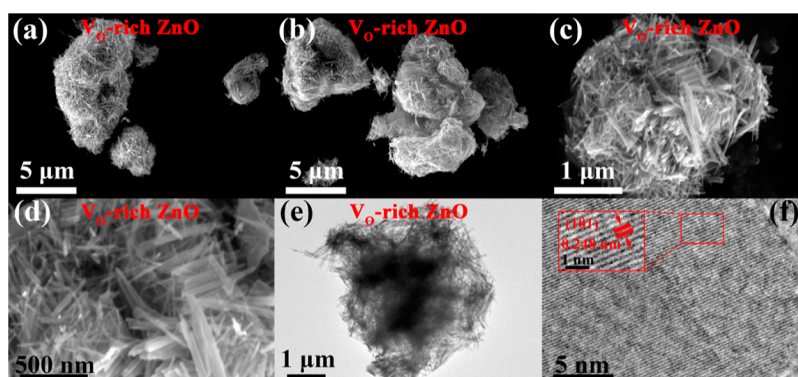
Figure 2. (a,b) Low-magnification SEM images of V_O-rich ZnO. (c,d) SEM images of V_O-rich ZnO with increasing magnifications. (e) TEM image of an isolated V_O-rich ZnO nanorod cluster. (f) HRTEM image of the V_O-rich ZnO crystal.
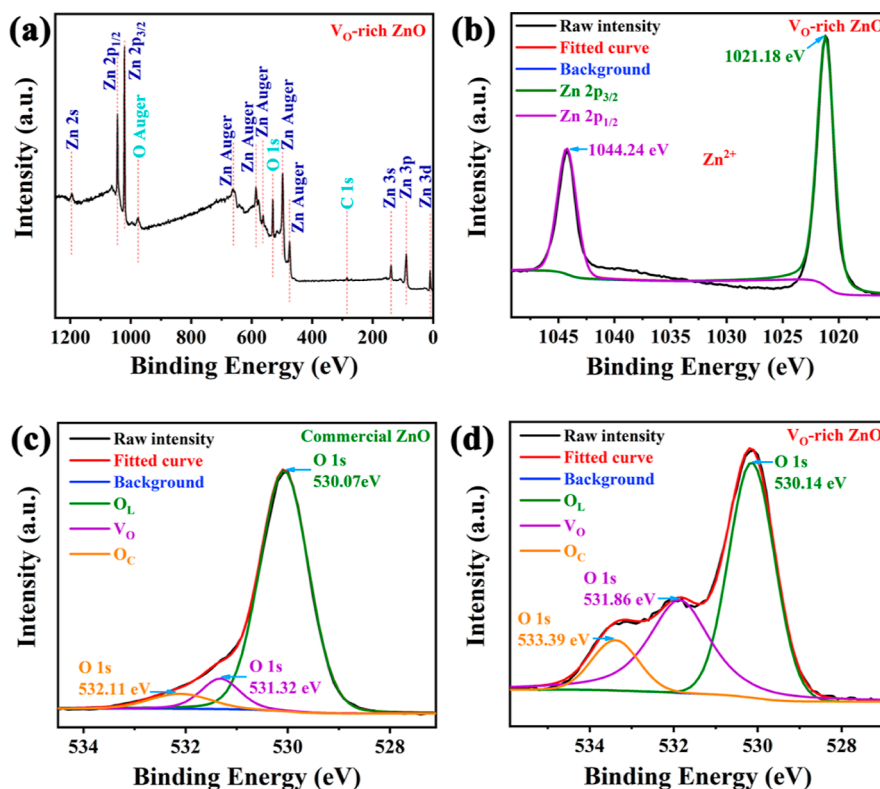
Figure 3. (a) Wide scan spectra and (b) high-resolution Zn 2p spectrum of V_O-rich ZnO. Deconvoluted O 1s core level spectra of (c) commercial ZnO and (d) V_O-rich ZnO.

on a permeable structure, which was regarded as an important feature in accelerating gas diffusion and reaction. As shown in Figure S3, the 3D structure and air permeability of ZnO clusters were maintained after the sample was coated on the sensor substrate. At last, the HRTEM test presented lattice fringes on the edge of a single ZnO nanorod. A fringe spacing of 0.248 nm identified in Figure 2f coincided well with the parameter of the (101) lattice plane of hexagonal ZnO, which also corresponded to the strongest XRD peak in Figure 1.

XPS analysis is one of the most effective methods to estimate the chemical states of the existing elements in one material. In Figure 3a, full-scan XPS spectra substantiated a series of constitutive orbit peaks of O and Zn elements situated at different binding energies, in addition to the fiducial C 1s peak at 284.8 eV. Markedly, sequential auger electron spectra (AES) of the Zn element with binding energies ranging from 400 to 700

eV were recorded. In high-resolution Figure 3b, two dominant peaks located at binding energies of 1021.18 and 1044.24 eV could be indexed to Zn $2p_{3/2}$ and $2p_{1/2}$,[1] respectively. Conventionally, the core level spectrum of O 1s could be fitted into three Gaussian function segments, that is, O_L, V_O, and O_C, using peak fit and deconvolution.[21] Treated spectra in Figure 3c,d unambiguously displayed cases of oxygen species in commercial and V_O-rich ZnO.

As is well known, oxygen species such as V_O and O_C are recognized as beneficial ingredients for enhancing gas-sensing performance of one material.[25] For intuition, some calculated data are listed in Table 1. As we could see, proportions for three oxygen species in commercial ZnO differed greatly from those in V_O-rich ZnO. Concretely speaking, the relative percentage of O_L dropped sharply from 84.57% in commercial ZnO to 52.36% in V_O-rich ZnO. Correspondingly, the total ratio of beneficial V_O

Table 1. Fitting Results of O 1s XPS Spectra of Commercial ZnO and V$_O$-Rich ZnO[a]

mater.	oxy.	B. E. (eV)	perc. (%)
commercial ZnO	O$_L$ (Zn−O)	530.07	84.57
	V$_O$ (vacancy)	531.32	9.21
	O$_C$ (chemisorbed)	532.11	6.22
VO-rich ZnO	O$_L$ (Zn−O)	530.14	52.36
	V$_O$ (vacancy)	531.86	36.27
	O$_C$ (chemisorbed)	533.39	11.37

[a]Mater.: materials; oxy.: oxygen species; B. E.: binding energy; and perc.: relative percentage.

and O$_C$ components in V$_O$-rich ZnO grew a lot. Particularly, the percentage of V$_O$ in V$_O$-rich ZnO reached up to 36.27%, 3.94 times as high as that in commercial ZnO. The ultrahigh V$_O$ percentage was the conspicuous sign and name origin of V$_O$-rich ZnO in this work and deemed to be strongly associated with the sensing mechanism concerning its follow-up visible light-activated HCHO gas-sensing performance.

In consideration of the tridimensional and air-permeable microstructure exhibited in Figure 2c,e, the specific surface area of V$_O$-rich ZnO deserved high expectation, the BET data of which are shown in Figure 4. The N$_2$ adsorption−desorption
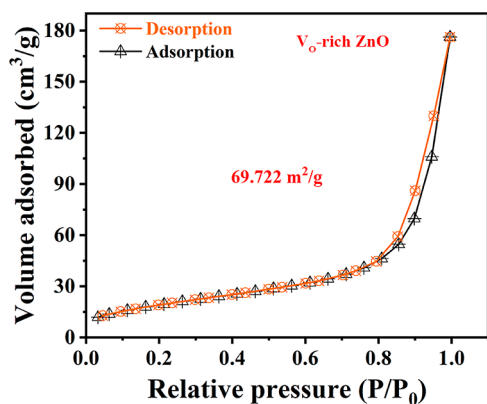

Figure 4. Nitrogen adsorption−desorption isotherm of V$_O$-rich ZnO.

isotherm curve represented a typical hysteresis loop from 0.8 to 1.0 (P/P_0). According to the IUPAC classification, the isotherm in Figure 4 roughly belonged to the type III form and exhibited a type H$_3$ hysteresis loop, which indicated that there did not exist an inherent and inerratic pore structure within V$_O$-rich ZnO. Correspondingly, the so-called holes reflected by the loop type

derived from the slit structure were formed by numerous interlaced nanorods in the clusters, consistent with the SEM and TEM observations hereinabove. The BET surface area of V$_O$-rich ZnO was measured to be 69.722 m^2/g, which was a high value and exactly conformed to our estimation. Besides, the high specific surface area of one material was advantageous to its gas-sensing performance.

UV−vis absorption spectroscopy is a direct way to grasp the spectral absorption range of one material. As mentioned in the Introduction, theoretically, intrinsic ZnO cannot be excited by visible light. As exhibited in Figure 5a, the initial absorption edge of commercial ZnO (green curve) was located at 352 nm (UV region). After a sharp decline period, the terminational absorption edge of commercial ZnO was 426 nm (visible region). Visibly, the spectral absorption range of commercial ZnO included the visible region (400−426 nm), slightly different from pure theoretical analysis. However, the falling range of commercial ZnO spectra between 400 and 426 nm was noticed to be very weak and could be ignored compared to the overall decline from 352 to 426 nm. In a word, the absorption range of commercial ZnO concentrated in the UV region. Also, the manifested weak visible absorption of commercial ZnO implied its lower band gap due to the existing defects, compared to intrinsic ZnO. Differently, the absorption spectra of V$_O$-rich ZnO possessed a much broader range, from 352 to 609 nm, than that of commercial ZnO. What was more, the absorption percentage within the visible region of V$_O$-rich ZnO was improved a lot. Therefore, the spectral utilization range was successfully extended to the visible region through introducing rich V$_O$ to ZnO, indicating the availability of V$_O$ engineering in band structure modulation.

PL spectroscopy is an effective means to evaluate the band gap and defect level of semiconductor materials through analyzing the wavelength and intensity of emitting light. Conventionally, PL spectra could be divided into the UV region (<400 nm) and visible region (400−700 nm). The intrinsic UV emission originated from excitonic recombination of near-band edge (NBE) electrons (at conduction band bottom) and holes (at valence band top).[71,72] In Figure 5b, commercial ZnO (green curve) displayed a sharp and narrow UV emission peak centered at 380 nm, through which we could calculate its band gap to be 3.26 eV,[20,73] very approaching the 3.37 eV of intrinsic ZnO. Correspondingly, the NBE emission peak of V$_O$-rich ZnO (red curve) became weaker and broader, also showing a red shift to a larger wavelength of 393 nm, which corresponded to a band gap of 3.16 eV. The estimation on band gaps of commercial and V$_O$-rich ZnO here was consistent with the abovementioned UV−vis
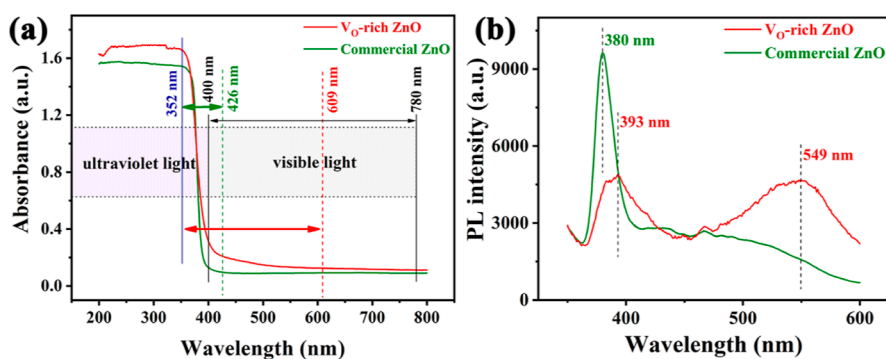
Figure 5. (a) UV−vis−NIR absorption and (b) PL spectroscopy of commercial and V$_O$-rich ZnO.

results. The larger decrease in band gap for V_O-rich ZnO could be ascribed to the massive introduction of defect states.

The visible emission region, including but not limited to the peak position, area, and/or intensity, is intensively directed to the defect level in one material. Clearly, a broad band centered at 549 nm (green light) could be detected in PL spectra of V_O-rich ZnO. As reported, green emission, attached to deep level emissions (DLE), was generated by the recombination of singly ionized oxygen vacancies (V_O^+) and photogenerated holes[74,75] or derived from structural defects such as zinc and oxygen vacancies, interstitial zinc and oxygen, and so forth.[73,76,77] Noteworthily, the peak area of green emission (549 nm) in V_O-rich ZnO outdistanced that of UV emission (393 nm), fully indicating the high percentage of defects in it. In contrast, no visible region emissions could be recognized in commercial ZnO, proving that the defect level of commercial ZnO was very low.

3.2. Gas-Sensing Properties. The selectivity of V_O-rich ZnO was first evaluated. As shown in Figure 6, under visible light
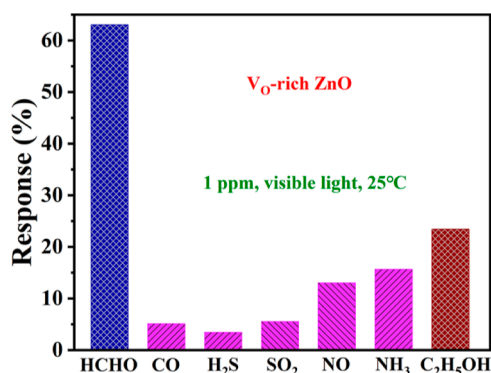
Figure 6. Responses of the sensor based on V_O-rich ZnO toward 1 ppm HCHO, CO, H_2S, SO_2, NO, NH_3, and C_2H_5OH under visible light irradiation at RT.

irradiation, V_O-rich ZnO exhibited responses toward some typical gases at RT. Distinctly, V_O-rich ZnO showed the highest response to HCHO and the second-highest response to ethanol under the abovementioned conditions. The response resolution ratio (R_{HCHO}/R_{H2S}) of V_O-rich ZnO could reach 18.5. In addition, the response ratio of HCHO to ethanol was still 2.7. From the abovementioned results, V_O-rich ZnO was verified to show a tendentious response toward HCHO compared to interferential gases. As reported,[78,79] photoinduced Zn^+ in ZnO could activate C−H bonds through oriented adsorption and charge transfer, for example, in photocatalytic oxidation of methane.[78] In view of the high activity of HCHO, V_O-rich ZnO was inclined to react with C−H bonds in HCHO under visible light irradiation, which might explain its high selectivity to some extent.

Sensing properties toward HCHO of sensors based on commercial and V_O-rich ZnO at RT in the dark or under visible light irradiation were compared in detail. As shown in Figure 7a, there was no recognizable response toward HCHO for commercial ZnO at RT in the dark, which conformed to general requirements for high detection temperature in VOC sensing. Consistent with the results in Figure 5a, visible light irradiation could activate commercial ZnO in this work, although a response of just 2.3% toward 1 ppm HCHO at RT shown in Figure 7b was far from satisfactory. As we could see,

commercial oxides, for example, ZnO, without any modification were unsuitable for detecting VOCs at RT as in most cases.

In contrast, in Figure 7c, although still not high, a response of 5.75% toward 1 ppm HCHO for V_O-rich ZnO in the dark was actually a huge step forward compared to the case of commercial ZnO in Figure 7a, which also proved the crucial role of rich V_O in RT HCHO sensing. However, without both thermal and optical excitation, the response/recovery time of V_O-rich ZnO when detecting HCHO was relatively long. Furthermore, as shown in Figure 7d, visible light irradiation fully activated the sensing potential of V_O-rich ZnO. At RT, the response of V_O-rich ZnO toward 1 ppm HCHO came up to 63% under visible light irradiation, 10.96 times as high as that in the dark. What was more, the response and recovery time of V_O-rich ZnO toward 1 ppm HCHO was drastically shortened to 32 and 20 s, respectively, at RT. Frankly speaking, such a response and recovery speed at RT was comparable to many sensors of the same kind working at high temperature. Obviously, when comparing results in Figure 7b,d, the concurrence of rich V_O and visible light irradiation generated an irrefutable effect on RT HCHO sensing parameters, confirming the feasibility of V_O enrichment in promoting visible light-activated gas-sensing performance.

The response−concentration property of the V_O-rich ZnO sensor was further examined under visible light irradiation at 25 °C. Figure 8a shows the obtained raw current data, proving the n-type nature of V_O-rich ZnO. Displaying an analogical form with those in Figure 8a, curves in Figure 8b provided variation tendencies of sensor response, response/recovery time. Consistent with the vast majority of cases, responses of V_O-rich ZnO grew gradually under HCHO with progressively elevated concentrations. In particular, response of V_O-rich ZnO toward 0.5 ppm HCHO remained 32%, indicating its great potential in low-concentration HCHO sensing. Moreover, response and recovery speeds of V_O-rich ZnO became increasingly faster toward HCHO from 0.5 to 10 ppm. For example, the response time of the V_O-rich ZnO sensor toward 5 and 10 ppm HCHO under visible light irradiation at 25 °C was 14 and 10 s, respectively. Correspondingly, the recovery time in the abovementioned cases was, respectively, 12 and 5 s. In comparison with results in Figure 7d, both the response and recovery times were greatly shortened in higher concentration of HCHO, manifesting faster reaction/desorption rates with more target gas molecules in the surrounding environment.

Generally speaking, moisture will generate a toxic effect on gas-sensitive reactions and suppress sensor response. When the operating temperature of a sensor is low, below the water boiling point (100 °C), for example, liquid water around the device will adhere to the surface of the sensitive material, covering local active sites and hindering considerable target gases from contact and reaction. When the device temperature is above 100 °C, gaseous water in the adjacent space will compete against target gases and squeeze the ratio of effective response. Conceivably, at RT, increasing moisture in the environment will exert a negative influence on the response of the V_O-rich ZnO sensor toward HCHO. As depicted in Figure 9, responses of V_O-rich ZnO toward HCHO showed a rapid downward trend when relative humidity of the testing environment was artificially elevated from 20 to 100%. Especially, the response of the sensor toward 1 ppm HCHO under 100% RH (visible light irradiation, RT) was only 26.5%, decaying by 58% compared to the initial value (63% under 20% RH). It served to show the consistent harmfulness of
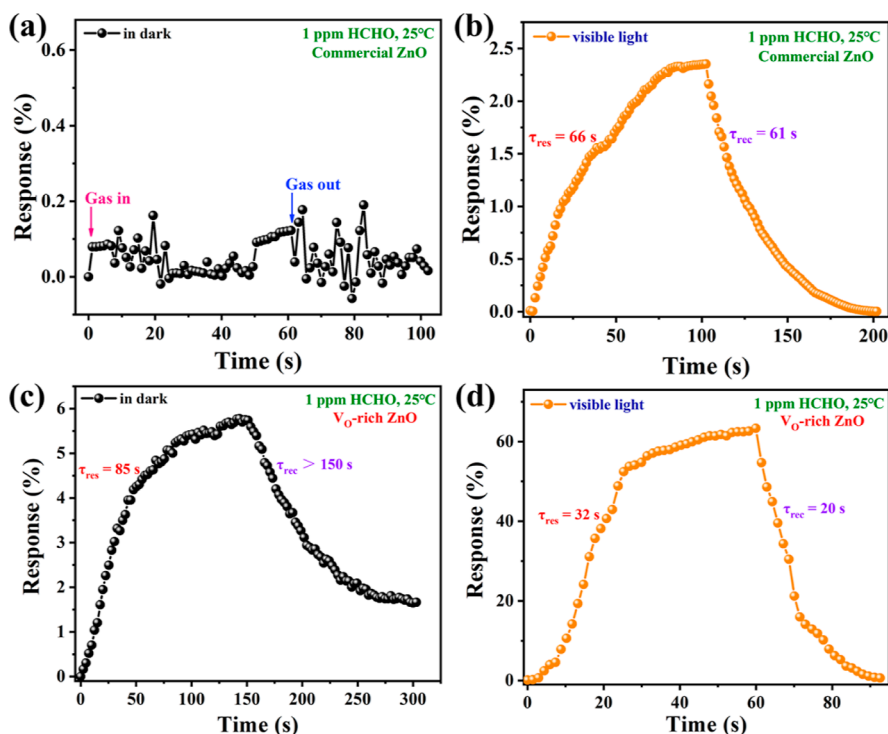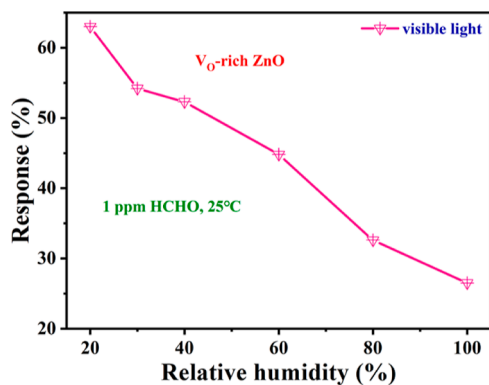
Figure 7. Single-cycle response−recovery transient curves of the sensor based on (a,b) commercial ZnO and (c,d) V_O-rich ZnO to 1 ppm HCHO at RT in the dark and under visible light irradiation.
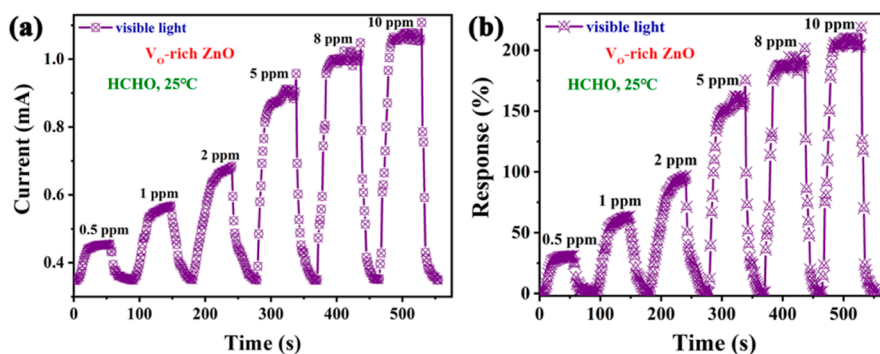
Figure 8. Dynamic response−recovery curves of (a) current and (b) response for the sensor based on V_O-rich ZnO to 0.5−10 ppm HCHO at RT under visible light irradiation.


Figure 9. Response−humidity relationship of the sensor based on V_O-rich ZnO at RT under visible light irradiation.

moisture to sensor response and helplessness of visible light irradiation in this process.

At last, records of the successive and long-term response characteristics of V_O-rich ZnO toward 1 ppm HCHO at RT under visible light irradiation are shown in Figure 10a,b. As shown in Figure 10a, response−recovery curves in four consecutive cycles maintained an absolute consistency, exhibiting the good repeatability of the sensor. More importantly, although the sampling responses lasting for 30 days in Figure 10b maintained a dynamic volatility, the ultimate response on the 30th day was almost equal to the initial value, proving the fine long-term stability of the sensor. In short, the above-mentioned conclusions reflected the objectivity and reliability of the V_O-rich ZnO sensor in data acquisition and possible practical application.

In addition, an all-around comparison between the sensing performance of the V_O-rich ZnO sensor fabricated in this work and other recent reports about HCHO gas sensors[13,22,39,70,80−86] is summarized in Table 2. The performance indexes showed by the V_O-rich ZnO sensor were considered to be pre-eminent on the whole.
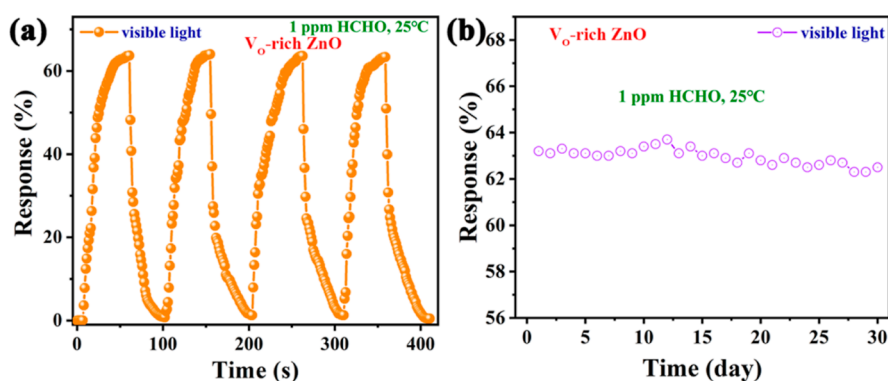
Figure 10. (a) Repeatedly cyclic response−recovery curves and (b) long-term stability tests of the sensor based on V_O-rich ZnO to 1 ppm HCHO at RT under visible light irradiation.

Table 2. Comparison of HCHO Sensing Performance in This Work and Those in Other Literature Studies[a]

mater.	temp. (°C)	L. S. (nm)	conc. (ppm)	res.	$\tau_{res.}/\tau_{recov.}$ (s)	Y.	ref.
$WO_3/ZnWO_4$	220		5	44.5[b]	12/14	2019	[13]
$Cu-Sn_3O_4$	160		100	53[b]	5/120	2020	[80]
$Y-SnO_2$	180		25	9[b]	8/10	2019	[81]
CuO	30		80	32[c]	301/705	2020	[39]
g-C_3N_4/ZnO	RT		50	24.4[b]	30/70	2020	[82]
Pt/MoO_3	RT		200	39.3%[d]	21.4/16.6	2019	[83]
PEDOT/PSS/MWCNTs-N_2	RT		10	30.5%[d]	45/7	2019	[84]
TiO_2/SnO_2	RT	UV (365)	10	20[b]	20/56	2020	[22]
ZnO_x/ANS/rGO	RT	vis. (405)	1	38%[d]	47/39	2021	[70]
$HoFeO_3$	RT	red (660)	100	75%[e]	719/248	2020	[85]
MoS_2/rGO	RT	vis. (>420)	10	64%[e]	17/98	2020	[86]
VO-rich ZnO	RT	vis. (>420)	1	63%[f]	32/20	this work	
			10	208%[f]	10/5		

[a]Mater.: materials; temp.: operating temperature; L. S.: light source; conc.: gas concentration; res.: response; D. L.: detection limit; $\tau_{res.}/\tau_{recov.}$: response/recovery time; Y.: publication year; ref.: references; and vis.: visible light. [b]R_a/R_g. [c]R_g/R_a. [d]$(R_a - R_g)/R_a*100\%$. [e]$(R_g - R_a)/R_a*100\%$. [f]$(I_g - I_a)/I_a*100\%$.

3.3. Gas-Sensing Mechanism.

For SMO-type gas sensors, from the current point of view, the adsorption and subsequent reactions of target molecules on/with sensing materials give rise to the change in carrier concentration, which constitutes the source of device response. In essence, under the same working temperature and gas concentration, the adsorption and ultimate reaction quantity, respectively, dependent on the microstructure and O_C content of sensing materials determines the response amplitude.

In this work, as shown in Figure 2a,b, a 3D microstructure of V_O-rich ZnO was obtained after microwave treatment. In addition, the high specific surface area of V_O-rich ZnO due to its 3D microstructure had been proved in the BET test in Figure 4. Therefore, under the same test conditions, the quantity of gas adsorption on V_O-rich ZnO was considered to be far more than that on commercial ZnO powders, which should be one motivator, but not the decisive factor, of the emerged HCHO response in Figure 7c.

As shown in Table 1, O_C content increased from 6.22% in commercial ZnO to 11.37% in V_O-rich ZnO, which was partially derived from the contribution of rich V_O. As described in the Introduction, V_O can act as electron donors and active sites, which conduces to both gas (including oxygen) adsorption and redox reactions. It followed that the abundance of V_O and resulting O_C content increase promoted together the adsorption and reaction quantity, which constituted the main cause of the RT sensing of V_O-rich ZnO toward HCHO in the dark.

Furthermore, a comparison between data in Figure 7a,b verified the consistent effectiveness of photoactivation in RT sensing. However, the response of commercial ZnO toward HCHO in Figure 7b was rather weak, even inferior to that of V_O-rich ZnO in the dark, due to its deficient visible light absorptivity proven in Figure 5a. As it turned out, the single photoexcitation in Figure 7b or V_O enrichment in Figure 7c was separately beneficial to the improvement of response/recovery properties or sensor response. As mentioned in the Introduction as well, V_O promotes light absorption and traps photoinduced electrons, which serves as a proof of the synergistic effect of V_O and light irradiation. Apparently, the performance in Figure 7d was not a simple superposition of those in Figure 7b,c, which substantiated the synergetic enhancement of V_O and visible light irradiation to sensor response. In addition, V_O extends the lifetime of light-activated carriers and favors the charge-transfer efficiency, which well explains the faster response/recovery speeds of the V_O-rich ZnO sensor under visible light irradiation in Figure 7d compared to those in Figure 7b.

4. CONCLUSIONS

In conclusion, 3D V_O-rich ZnO was successfully prepared through microwave heating. Through a series of characterizations, V_O-rich ZnO consisting of nanorod clusters was proved to possess a gas-permeability structure and high BET surface area. What is more, the V_O content in V_O-rich ZnO was found to increase by a wide margin compared to that in commercial ZnO.

It was just the rich V_O in V_O-rich ZnO that led to its superior RT HCHO sensing properties under visible light irradiation. At last, the mechanism of gas sensitivity enhancement was proposed based on the available data in this work. The role of V_O in light-activated gas-sensing performance was consolidated in this work, which is of certain reference significance to related research.

■ ASSOCIATED CONTENT

Ⓢ Supporting Information

The Supporting Information is available free of charge at https://pubs.acs.org/doi/10.1021/acsomega.2c02613.

> Photographs of the signal acquisition section; HRTEM image of a part of one single ZnO nanorod; and SEM image of ZnO nanorods coated on the sensor substrate (PDF)

■ AUTHOR INFORMATION

Corresponding Authors

Jing Wang − *Key Laboratory of Synthetic and Biological Colloids (Ministry of Education), School of Chemical and Material Engineering, Jiangnan University, Wuxi 214122, China*; Email: jingwang@jiangnan.edu.cn

Yi Xia − *Research Center for Analysis and Measurement, Kunming University of Science and Technology, and Analytic & Testing Research Center of Yunnan, Kunming 650093, China*; Ⓞ orcid.org/0000-0003-3186-308X; Email: xiayi0125@163.com

Authors

Bo Zhang − *Engineering Research Center of IoT Technology Applications (Ministry of Education), Department of Electronic Engineering, Institute of Advanced Technology, Jiangnan University, Wuxi 214122, China*

Qufu Wei − *Key Laboratory of Eco-Textiles (Ministry of Education), Jiangnan University, Wuxi 214122, China*; Ⓞ orcid.org/0000-0003-2143-9939

Pingping Yu − *Engineering Research Center of IoT Technology Applications (Ministry of Education), Department of Electronic Engineering, Institute of Advanced Technology, Jiangnan University, Wuxi 214122, China*

Shuai Zhang − *Engineering Research Center of IoT Technology Applications (Ministry of Education), Department of Electronic Engineering, Institute of Advanced Technology, Jiangnan University, Wuxi 214122, China*

Yin Xu − *Engineering Research Center of IoT Technology Applications (Ministry of Education), Department of Electronic Engineering, Institute of Advanced Technology, Jiangnan University, Wuxi 214122, China*

Yue Dong − *Engineering Research Center of IoT Technology Applications (Ministry of Education), Department of Electronic Engineering, Institute of Advanced Technology, Jiangnan University, Wuxi 214122, China*

Yi Ni − *Engineering Research Center of IoT Technology Applications (Ministry of Education), Department of Electronic Engineering, Institute of Advanced Technology, Jiangnan University, Wuxi 214122, China*

Jinping Ao − *Engineering Research Center of IoT Technology Applications (Ministry of Education), Department of Electronic Engineering, Institute of Advanced Technology, Jiangnan University, Wuxi 214122, China*

Complete contact information is available at:

https://pubs.acs.org/10.1021/acsomega.2c02613

Notes

The authors declare no competing financial interest.

■ REFERENCES

(1) Liu, Y.; Zhang, J.; Li, G.; Liu, J.; Liang, Q.; Wang, H.; Zhu, Y.; Gao, J.; Lu, H. In$_2$O$_3$-ZnO nanotubes for the sensitive and selective detection of ppb-level NO$_2$ under UV irradiation at room temperature. *Sens. Actuators, B* **2022**, *355*, 131322.

(2) Yuan, Z.; Zhao, Q.; Xie, C.; Liang, J.; Duan, X.; Duan, Z.; Li, S.; Jiang, Y.; Tai, H. Gold-loaded tellurium nanobelts gas sensor for ppt-level NO$_2$ detection at room temperature. *Sens. Actuators, B* **2022**, *355*, 131300.

(3) Xu, K.; Ha, N.; Hu, Y.; Ma, Q.; Chen, W.; Wen, X.; Ou, R.; Trinh, V.; McConville, C. F.; Zhang, B. Y.; Ren, G.; Ou, J. Z. A room temperature all-optical sensor based on two-dimensional SnS$_2$ for highly sensitive and reversible NO$_2$ sensing. *J. Hazard. Mater.* **2022**, *426*, 127813.

(4) Liang, J.; Wu, W.; Lou, Q.; Wang, K.; Xuan, C. Room temperature NO$_2$ sensing performance of Ag nanoparticles modified VO$_2$ nanorods. *J. Alloys Compd.* **2021**, *890*, 161837.

(5) Sheikh, A. D.; Vhanalakar, V. K.; Katware, A. S.; Pawar, K. K.; Kulkarni, S. K. Ultrasensitive organic-inorganic nanotube thin films of halogenated perovskites as room temperature ammonia sensors. *J. Alloys Compd.* **2022**, *894*, 162388.

(6) Wu, Z.; Liang, L.; Zhu, S.; Guo, Y.; Yao, Y.; Yang, Y.; Gu, S.; Zhou, Z. High Sensitivity of Ammonia Sensor through 2D Black Phosphorus/Polyaniline Nanocomposite. *Nanomaterials* **2021**, *11*, 3026.

(7) Kanaparthi, S.; Singh, S. G. MoS$_2$ chemiresistive sensor array on paper patterned with toner lithography for simultaneous detection of NH$_3$ and H$_2$S gases. *ACS Sustainable Chem. Eng.* **2021**, *9*, 14735−14743.

(8) Zhang, C.; Wu, K.; Liao, H.; Debliquy, M. Room temperature WO$_3$-Bi$_2$WO$_6$ sensors based on hierarchical microflowers for ppb-level H$_2$S detection. *Chem. Eng. J.* **2022**, *430*, 132813.

(9) Tang, J.; Wang, H.; Wang, X.; Xie, C.; Zeng, D. Prussian blue-derived hollow cubic α-Fe$_2$O$_3$ for highly sensitive room temperature detection of H$_2$S. *Sens. Actuators, B* **2022**, *351*, 130954.

(10) Zhang, W.; Wang, X.; Fan, Z.; Li, J.; Liu, G.; Lv, X.; Li, B.; Zhou, J.; Xie, E.; Zhang, Z. Switching effect of p-CuO nanotube/n-In$_2$S$_3$ nanosheet heterostructures for high-performance room-temperature H$_2$S sensing. *ACS Appl. Mater. Interfaces* **2021**, *13*, 52938−52949.

(11) Zhang, X.; Lan, W.; Xu, J.; Luo, Y.; Pan, J.; Liao, C.; Yang, L.; Tan, W.; Huang, X. ZIF-8 derived hierarchical hollow ZnO nanocages with quantum dots for sensitive ethanol gas detection. *Sens. Actuators, B* **2019**, *289*, 144−152.

(12) Chang, X.; Xu, S.; Liu, S.; Wang, N.; Sun, S.; Zhu, X.; Li, J.; Ola, O.; Zhu, Y. Highly sensitive acetone sensor based on WO$_3$ nanosheets derived from WS$_2$ nanoparticles with inorganic fullerene-like structures. *Sens. Actuators, B* **2021**, *343*, 130135.

(13) Li, H.; Chu, S.; Ma, Q.; Wang, J.; Che, Q.; Wang, G.; Yang, P. Hierarchical WO$_3$/ZnWO$_4$ 1D fibrous heterostructures with tunable in-situ growth of WO$_3$ nanoparticles on surface for efficient low concentration HCHO detection. *Sens. Actuators, B* **2019**, *286*, 564−574.

(14) Salimi kuchi, P.; Roshan, H.; Sheikhi, M. H. A novel room temperature ethanol sensor based on PbS:SnS$_2$ nanocomposite with

enhanced ethanol sensing properties. *J. Alloys Compd.* **2020**, *816*, 152666.

(15) Vishwakarma, A. K.; Sharma, A. K.; Yadav, N. K.; Yadava, L. Development of CdS-doped TiO_2 nanocomposite as acetone gas sensor. *Vacuum* **2021**, *191*, 110363.

(16) Subin David, S. P.; Veeralakshmi, S.; Sandhya, J.; Nehru, S.; Kalaiselvam, S. Room temperature operatable high sensitive toluene gas sensor using chemiresistive Ag/Bi_2O_3 nanocomposite. *Sens. Actuators, B* **2020**, *320*, 128410.

(17) Wongchoosuk, C.; Subannajui, K.; Wang, C.; Yang, Y.; Güder, F.; Kerdcharoen, T.; Cimalla, V.; Zacharias, M. Electronic nose for toxic gas detection based on photostimulated core-shell nanowires. *RSC Adv.* **2014**, *4*, 35084−35088.

(18) Eom, T. H.; Cho, S. H.; Suh, J. M.; Kim, T.; Lee, T. H.; Jun, S. E.; Yang, J. W.; Lee, J.; Hong, S.-H.; Jang, H. W. Substantially improved room temperature NO_2 sensing in 2-dimensional SnS_2 nanoflowers enabled by visible light illumination. *J. Mater. Chem. A* **2021**, *9*, 11168−11178.

(19) Reddeppa, M.; Nam, D.-J.; Bak, N.-h.; Pasupuleti, K. S.; Woo, H.; Kim, S.-G.; Oh, J.-E.; Kim, M.-D. Proliferation of the light and gas interaction with GaN nanorods grown on a V-grooved Si(111) substrate for UV photodetector and NO_2 gas sensor applications. *ACS Appl. Mater. Interfaces* **2021**, *13*, 30146−30154.

(20) Espid, E.; Noce, A. S.; Taghipour, F. The effect of radiation parameters on the performance of photo-activated gas sensors. *J. Photochem. Photobiol., A* **2019**, *374*, 95−105.

(21) Zou, Z.; Qiu, Y.; Xie, C.; Xu, J.; Luo, Y.; Wang, C.; Yan, H. CdS/TiO_2 nanocomposite film and its enhanced photoelectric responses to dry air and formaldehyde induced by visible light at room temperature. *J. Alloys Compd.* **2015**, *645*, 17−23.

(22) Zhang, S.; Zhao, L.; Huang, B.; Li, X. UV-activated formaldehyde sensing properties of hollow $TiO_2@SnO_2$ heterojunctions at room temperature. *Sens. Actuators, B* **2020**, *319*, 128264.

(23) Cui, J.; Shi, L.; Xie, T.; Wang, D.; Lin, Y. UV-light illumination room temperature HCHO gas-sensing mechanism of ZnO with different nanostructures. *Sens. Actuators, B* **2016**, *227*, 220−226.

(24) Zou, Z.; Qiu, Y.; Xu, J.; Guo, P.; Luo, Y.; Wang, C. Enhanced formaldehyde photoelectric response on ZnO film illuminated with visible light. *J. Alloys Compd.* **2017**, *695*, 2117−2123.

(25) Zhang, B.; Bao, N.; Wang, T.; Xu, Y.; Dong, Y.; Ni, Y.; Yu, P.; Wei, Q.; Wang, J.; Guo, L.; Xia, Y. High-performance room temperature NO_2 gas sensor based on visible light irradiated In_2O_3 nanowires. *J. Alloys Compd.* **2021**, *867*, 159076.

(26) Deng, L.; Ding, X.; Zeng, D.; Tian, S.; Li, H.; Xie, C. Visible-light activate mesoporous WO_3 sensors with enhanced formaldehyde-sensing property at room temperature. *Sens. Actuators, B* **2012**, *163*, 260−266.

(27) Zhai, J.; Wang, D.; Peng, L.; Lin, Y.; Li, X.; Xie, T. Visible-light-induced photoelectric gas sensing to formaldehyde based on CdS nanoparticles/ZnO heterostructures. *Sens. Actuators, B* **2010**, *147*, 234−240.

(28) Liu, D.; Tang, Z.; Zhang, Z. Visible light assisted room-temperature NO_2 gas sensor based on hollow $SnO_2@SnS_2$ nanostructures. *Sens. Actuators, B* **2020**, *324*, 128754.

(29) Zhang, B.; Liu, G.; Cheng, M.; Gao, Y.; Zhao, L.; Li, S.; Liu, F.; Yan, X.; Zhang, T.; Sun, P.; Lu, G. The preparation of reduced graphene oxide-encapsulated α-Fe_2O_3 hybrid and its outstanding NO_2 gas sensing properties at room temperature. *Sens. Actuators, B* **2018**, *261*, 252−263.

(30) Song, X.; Li, L.; Chen, X.; Xu, Q.; Song, B.; Pan, Z.; Liu, Y.; Juan, F.; Xu, F.; Cao, B. Enhanced triethylamine sensing performance of α-Fe_2O_3 nanoparticle/ZnO nanorod heterostructures. *Sens. Actuators, B* **2019**, *298*, 126917.

(31) Zhang, D.; Wu, D.; Cao, Y.; Zong, X.; Yang, Z. Construction of Co_3O_4 nanorods/In_2O_3 nanocubes heterojunctions for efficient sensing of NO_2 gas at low temperature. *J. Mater. Sci.: Mater. Electron.* **2018**, *29*, 19558−19566.

(32) Zhang, L.; Gao, Z.; Liu, C.; Zhang, Y.; Tu, Z.; Yang, X.; Yang, F.; Wen, Z.; Zhu, L.; Liu, R.; Li, Y.; Cui, L. Synthesis of TiO_2 decorated

Co_3O_4 acicular nanowire arrays and their application as an ethanol sensor. *J. Mater. Chem. A* **2015**, *3*, 2794−2801.

(33) Souissi, R.; Bouguila, N.; Labidi, A. Ethanol sensing properties of sprayed β-In_2S_3 thin films. *Sens. Actuators, B* **2018**, *261*, 522−530.

(34) Wang, X.; Zhou, C.; Wang, W.; Du, B.; Cai, J.; Feng, G.; Zhang, R. CdSe nanoparticle-sensitized ZnO sheets for enhanced photo-catalytic hydrogen evolution rates. *J. Alloys Compd.* **2018**, *747*, 826−833.

(35) Ho, W.; Yu, J. C. Sonochemical synthesis and visible light photocatalytic behavior of CdSe and CdSe/TiO_2 nanoparticles. *J. Mol. Catal. A: Chem.* **2006**, *247*, 268−274.

(36) Song, Y.; Li, N.; Chen, D.; Xu, Q.; Li, H.; He, J.; Lu, J. N-Doped and CdSe-sensitized 3D-ordered TiO_2 inverse opal films for synergistically enhanced photocatalytic performance. *ACS Sustainable Chem. Eng.* **2018**, *6*, 4000−4007.

(37) Niu, M.; Cao, D.; Sui, K.; Liu, C. InP/TiO_2 heterojunction for photoelectrochemical water splitting under visible-light. *Int. J. Hydrogen Energy* **2020**, *45*, 11615−11624.

(38) Chizhov, A. S.; Mordvinova, N. E.; Rumyantseva, M. N.; Krylov, I. V.; Drozdov, K. A.; Li, X.; Gas'kov, A. M. The Effect of CdSe and InP Quantum Dots on the Interaction of ZnO with NO_2 under Visible Light Irradiation. *Russ. J. Inorg. Chem.* **2018**, *63*, 512−518.

(39) Zi, B.; Chen, M.; Zhang, Y.; Rong, Q.; Hu, J.; Wang, H.; He, J.; Zhou, S.; Zhang, D.; Zhang, J.; Liu, Q. Morphology-dependent formaldehyde detection of porous copper oxide hierarchical micro-spheres at near-room temperature. *Microporous Mesoporous Mater.* **2020**, *302*, 110232.

(40) Kim, J.-S.; Yoo, H.-W.; Choi, H. O.; Jung, H.-T. Tunable volatile organic compounds sensor by using thiolated ligand conjugation on MoS_2. *Nano Lett.* **2014**, *14*, 5941−5947.

(41) Zhou, Y.; Itoh, H.; Uemura, T.; Naka, K.; Chujo, Y. Preparation, optical spectroscopy, and electrochemical studies of novel π-conjugated polymer-protected stable PbS colloidal nanoparticles in a nonaqueous solution. *Langmuir* **2002**, *18*, 5287−5292.

(42) Han, L.; Wang, D.; Cui, J.; Chen, L.; Jiang, T.; Lin, Y. Study on formaldehyde gas-sensing of In_2O_3-sensitized ZnO nanoflowers under visible light irradiation at room temperature. *J. Mater. Chem.* **2012**, *22*, 12915−12920.

(43) Wang, J.; Fan, S.; Xia, Y.; Yang, C.; Komarneni, S. Room-temperature gas sensors based on ZnO nanorod/Au hybrids: Visiblelight-modulated dual selectivity to NO_2 and NH_3. *J. Hazard. Mater.* **2020**, *381*, 120919.

(44) Zhang, Q.; Xie, G.; Xu, M.; Su, Y.; Tai, H.; Du, H.; Jiang, Y. Visible light-assisted room temperature gas sensing with ZnO-Ag heterostructure nanoparticles. *Sens. Actuators, B* **2018**, *259*, 269−281.

(45) Xia, Y.; Wang, J.; Xu, L.; Li, X.; Huang, S. A room-temperature methane sensor based on Pd-decorated ZnO/rGO hybrids enhanced by visible light photocatalysis. *Sens. Actuators, B* **2020**, *304*, 127334.

(46) Joshi, S.; Kumar, R.; Jones, L. A.; Mayes, E. L. H.; Ippolito, S. J.; Sunkara, M. V. Modulating interleaved ZnO assembly with CuO nanoleaves for multifunctional performance: perdurable CO_2 gas sensor and visible light catalyst. *Inorg. Chem. Front.* **2017**, *4*, 1848−1861.

(47) Sun, Q.; Li, Y.; Hao, J.; Zheng, S.; Zhang, T.; Wang, T.; Wu, R.; Fang, H.; Wang, Y. Increased active sites and charge transfer in the SnS_2/TiO_2 heterostructure for visible-light-assisted NO_2 sensing. *ACS Appl. Mater. Interfaces* **2021**, *13*, 54152−54161.

(48) Wu, C.-H.; Chou, T.-L.; Wu, R.-J. Rapid detection of trace ozone in TiO_2-In_2O_3 materials by using the differential method. *Sens. Actuators, B* **2018**, *255*, 117−124.

(49) Yang, Z.; Guo, L.; Zu, B.; Guo, Y.; Xu, T.; Dou, X. CdS/ZnO core/shell nanowire-built films for enhanced photodetecting and optoelectronic gas-sensing applications. *Adv. Opt. Mater.* **2014**, *2*, 738−745.

(50) Chizhov, A. S.; Rumyantseva, M. N.; Vasiliev, R. B.; Filatova, D. G.; Drozdov, K. A.; Krylov, I. V.; Marchevsky, A. V.; Karakulina, O. M.; Abakumov, A. M.; Gaskov, A. M. Visible light activation of room temperature NO_2 gas sensors based on ZnO, SnO_2 and In_2O_3 sensitized with CdSe quantum dots. *Thin Solid Films* **2016**, *618*, 253−262.

(51) Geng, X.; Zhang, C.; Debliquy, M. Cadmium sulfide activated zinc oxide coatings deposited by liquid plasma spray for room temperature nitrogen dioxide detection under visible light illumination. *Ceram. Int.* **2016**, *42*, 4845−4852.

(52) Chizhov, A. S.; Rumyantseva, M. N.; Vasiliev, R. B.; Filatova, D. G.; Drozdov, K. A.; Krylov, I. V.; Abakumov, A. M.; Gaskov, A. M. Visible light activated room temperature gas sensors based on nanocrystalline ZnO sensitized with CdSe quantum dots. *Sens. Actuators, B* **2014**, *205*, 305−312.

(53) Wang, H.; Bai, J.; Dai, M.; Liu, K.; Liu, Y.; Zhou, L.; Liu, F.; Liu, F.; Gao, Y.; Yan, X.; Geyu, L. Visible light activated excellent NO_2 sensing based on 2D/2D ZnO/g-C_3N_4 heterojunction composites. *Sens. Actuators, B* **2020**, *304*, 127287.

(54) Kwak, C. H.; Im, U.-S.; Seo, S. W.; Kim, M. I.; Huh, Y. S.; Im, J. S. Effects of carbon doping on TiO_2 for enhanced visible light-driven NO sensing performance. *Mater. Lett.* **2021**, *288*, 129313.

(55) Khosravi, Y.; Sasar, M.; Abdi, Y. Light-induced oxygen sensing using ZnO/GO based gas sensor. *Mater. Sci. Semicond. Process.* **2018**, *85*, 9−14.

(56) Tian, X.; Yang, X.; Yang, F.; Qi, T. A visible-light activated gas sensor based on perylenediimide-sensitized SnO_2 for NO_2 detection at room temperature. *Colloids Surf., A* **2019**, *578*, 123621.

(57) Huang, J.; Jiang, D.; Zhou, J.; Ye, J.; Sun, Y.; Li, X.; Geng, Y.; Wang, J.; Du, Y.; Qian, Z. Visible light-activated room temperature NH_3 sensor base on CuPc-loaded ZnO nanorods. *Sens. Actuators, B* **2021**, *327*, 128911.

(58) Yu, Y.; Yao, B.; He, Y.; Cao, B.; Ma, W.; Chang, L. Oxygen defect-rich In-doped ZnO nanostructure for enhanced visible light photo-catalytic activity. *Mater. Chem. Phys.* **2020**, *244*, 122672.

(59) Zhang, C.; Liu, G.; Geng, X.; Wu, K.; Debliquy, M. Metal oxide semiconductors with highly concentrated oxygen vacancies for gas sensing materials: A review. *Sens. Actuators, A* **2020**, *309*, 112026.

(60) Wang, J.; Chen, R.; Xiang, L.; Komarneni, S. Synthesis, properties and applications of ZnO nanomaterials with oxygen vacancies: A review. *Ceram. Int.* **2018**, *44*, 7357−7377.

(61) Wang, Z.; Miao, J.; Zhang, H.; Wang, D.; Sun, J. Hollow cubic $ZnSnO_3$ with abundant oxygen vacancies for H_2S gas sensing. *J. Hazard. Mater.* **2020**, *391*, 122226.

(62) Zhang, C.; Geng, X.; Li, J.; Luo, Y.; Lu, P. Role of oxygen vacancy in tuning of optical, electrical and NO_2 sensing properties of ZnO_{1-x} coatings at room temperature. *Sens. Actuators, B* **2017**, *248*, 886−893.

(63) Peng, S.; Wang, Z.; Liu, R.; Bi, J.; Wu, J. Controlled oxygen vacancies of $ZnFe_2O_4$ with superior gas sensing properties prepared via a facile one-step self-catalyzed treatment. *Sens. Actuators, B* **2019**, *288*, 649−655.

(64) Liu, S.; Gao, S.; Wang, Z.; Fei, T.; Zhang, T. Oxygen vacancy modulation of commercial SnO_2 by an organometallic chemistry-assisted strategy for boosting acetone sensing performances. *Sens. Actuators, B* **2019**, *290*, 493−502.

(65) Al-Hashem, M.; Akbar, S.; Morris, P. Role of oxygen vacancies in nanostructured metal-oxide gas sensors: A review. *Sens. Actuators, B* **2019**, *301*, 126845.

(66) Ri, J.; Li, X.; Shao, C.; Liu, Y.; Han, C.; Li, X.; Liu, Y. Sn-doping induced oxygen vacancies on the surface of the In_2O_3 nanofibers and their promoting effect on sensitive NO_2 detection at low temperature. *Sens. Actuators, B* **2020**, *317*, 128194.

(67) Ma, M.; Peng, L.; Li, J.; Zhang, Y.; Wang, Z.; Bi, J.; Gao, D.; Wu, J. Oxygen vacancy engineering and superior sensing properties of hematite prepared via a one-step treatment. *Sens. Actuators, B* **2021**, *339*, 129907.

(68) Tong, B.; Meng, G.; Deng, Z.; Horprathum, M.; Klamchuen, A.; Fang, X. Surface oxygen vacancy defect engineering of p-$CuAlO_2$ via Ar&H_2 plasma treatment for enhancing VOCs sensing performances. *Chem. Commun.* **2019**, *55*, 11691−11694.

(69) Gurylev, V.; Perng, T. P. Defect engineering of ZnO: Review on oxygen and zinc vacancies. *J. Eur. Ceram. Soc.* **2021**, *41*, 4977−4996.

(70) Liang, H.; Guo, L.; Cao, N.; Hu, H.; Li, H.; Frans de Rooij, N.; Umar, A.; Algarni, H.; Wang, Y.; Zhou, G. Practical room temperature formaldehyde sensing based on a combination of visible-light activation and dipole modification. *J. Mater. Chem. A* **2021**, *9*, 23955−23967.

(71) Srinivasan, P.; Prakalya, D.; Jeyaprakash, B. G. UV-activated ZnO/CdO n-n isotype heterostructure as breath sensor. *J. Alloys Compd.* **2020**, *819*, 152985.

(72) Liu, Y.; Zhang, Q.; Yuan, H.; Luo, K.; Li, J.; Hu, W.; Pan, Z.; Xu, M.; Xu, S.; Levchenko, I.; Bazaka, K. Comparative study of photocatalysis and gas sensing of ZnO/Ag nanocomposites synthesized by one- and two-step polymer-network gel processes. *J. Alloys Compd.* **2021**, *868*, 158723.

(73) Hsu, C.-L.; Chang, L.-F.; Hsueh, T.-J. Light-activated humidity and gas sensing by ZnO nanowires grown on LED at room temperature. *Sens. Actuators, B* **2017**, *249*, 265−277.

(74) Basnet, P.; Samanta, D.; Chanu, T. I.; Chatterjee, S. Visible light facilitated degradation of alternate dye solutions by highly reusable Mn-ZnO nano-photocatalyst. *J. Alloys Compd.* **2021**, *867*, 158870.

(75) Li, F.; Jiang, Y.; Hu, L.; Liu, L.; Li, Z.; Huang, X. Structural and luminescent properties of ZnO nanorods and ZnO/ZnS nano-composites. *J. Alloys Compd.* **2009**, *474*, 531−535.

(76) Sun, G.; Cao, M.; Wang, Y.; Hu, C.; Liu, Y.; Ren, L.; Pu, Z. Anionic surfactant-assisted hydrothermal synthesis of high-aspect-ratio ZnO nanowires and their photoluminescence property. *Mater. Lett.* **2006**, *60*, 2777−2782.

(77) Choi, H.-S.; Vaseem, M.; Kim, S. G.; Im, Y.-H.; Hahn, Y.-B. Growth of high aspect ratio ZnO nanorods by solution process: Effect of polyethyleneimine. *J. Solid State Chem.* **2012**, *189*, 25−31.

(78) Chen, X.; Li, Y.; Pan, X.; Cortie, D.; Huang, X.; Yi, Z. Photocatalytic oxidation of methane over silver decorated zinc oxide nanocatalysts. *Nat. Commun.* **2016**, *7*, 12273.

(79) Li, L.; Li, G.-D.; Yan, C.; Mu, X.-Y.; Pan, X.-L.; Zou, X.-X.; Wang, K.-X.; Chen, J.-S. Efficient sunlight-driven dehydrogenative coupling of methane to ethane over a Zn^+-modified zeolite. *Angew. Chem., Int. Ed.* **2011**, *50*, 8299−8303.

(80) Wang, L.; Li, Y.; Yue, W.; Gao, S.; Zhang, C.; Chen, Z. High-performance formaldehyde gas sensor based on Cu-doped Sn_3O_4 hierarchical nanoflowers. *IEEE Sens. J.* **2020**, *20*, 6945−6953.

(81) Zhu, K.; Ma, S.; Tie, Y.; Zhang, Q.; Wang, W.; Pei, S.; Xu, X. Highly sensitive formaldehyde gas sensors based on Y-doped SnO_2 hierarchical flower-shaped nanostructures. *J. Alloys Compd.* **2019**, *792*, 938−944.

(82) David, S. P. S.; Veeralakshmi, S.; Nehru, S.; Kalaiselvam, S. A highly sensitive, selective and room temperature operable form-aldehyde gas sensor using chemiresistive g-C_3N_4/ZnO. *Mater. Adv.* **2020**, *1*, 2781−2788.

(83) Fu, X.; Yang, P.; Xiao, X.; Zhou, D.; Huang, R.; Zhang, X.; Cao, F.; Xiong, J.; Hu, Y.; Tu, Y.; Zou, Y.; Wang, Z.; Gu, H. Ultra-fast and highly selective room-temperature formaldehyde gas sensing of Pt-decorated MoO_3 nanobelts. *J. Alloys Compd.* **2019**, *797*, 666−675.

(84) Timsorn, K.; Wongchoosuk, C. Inkjet printing of room-temperature gas sensors for identification of formalin contamination in squids. *J. Mater. Sci.: Mater. Electron.* **2019**, *30*, 4782−4791.

(85) Song, Y.; Zhang, Y.; Ma, M.; Ren, J.; Liu, C.; Tan, J. Visible light-assisted formaldehyde sensor based on $HoFeO_3$ nanoparticles with sub-ppm detection limit. *Ceram. Int.* **2020**, *46*, 16337−16344.

(86) Wang, J.; Deng, H.; Li, X.; Yang, C.; Xia, Y. Visible-light photocatalysis enhanced room-temperature formaldehyde gas sensing by MoS_2/rGO hybrids. *Sens. Actuators, B* **2020**, *304*, 127317.